

## Synthesis and Properties of $\text{BaZr}_{0.1}\text{Ce}_{0.7}\text{Y}_{0.2-x}\text{M}_x\text{O}_{3-\delta}$ ( $x = 0, 0.1$ ; $\text{M} = \text{Dy}, \text{Yb}$ ) Compounds

R. Muccillo, E. N. S. Muccillo

Center of Science and Technology of Materials, Energy and Nuclear Research Institute  
C.P. 11049 - Pinheiros, S. Paulo, SP 05422-970, Brazil

The following barium cerate zirconate compounds were prepared by the solid state route:  $\text{BaZr}_{0.1}\text{Ce}_{0.7}\text{Y}_{0.2}\text{O}_{3-\delta}$ ,  $\text{BaZr}_{0.1}\text{Ce}_{0.7}\text{Dy}_{0.2}\text{O}_{3-\delta}$  and  $\text{BaZr}_{0.1}\text{Ce}_{0.7}\text{Y}_{0.1}\text{Dy}_{0.1}\text{O}_{3-\delta}$ . The powders were attrition milled, pressed and sintered at  $1550^\circ\text{C}/4$  h. X-ray diffraction data of all compositions show the perovskite orthorhombic phase (powders) and the perovskite cubic phase (pellets). Impedance spectroscopy measurements in the 5 Hz-13 MHz frequency range show that Dy may substitute totally or partially for Y without noticeable change in the electrical conductivity, whereas Yb substitution leads to a decrease in the electrical conductivity. The bulk electrical resistivity follows the trend:  $\text{Yb-} < \text{Dy-} < \text{Dy-Y-} < \text{Yb-Y-} < \text{Y-}$  doped barium cerate zirconate sintered ceramics. A detailed scanning probe microscopy analysis of the polished and thermally etched surfaces of the sintered pellets show images of sub-intergranular regions, which are further evidences of the large grain boundary electrical resistivity of barium cerate compounds.

### Introduction

Ceramic protonic conductors based on barium cerate-zirconate compounds doped with yttrium or rare-earth elements have been proposed as candidates for solid oxide fuel cells operating at temperatures lower than those used in SOFC devices with yttria-stabilized zirconia as solid electrolyte (1-7). The main problems to overcome for using barium cerate, barium zirconate and barium cerate zirconate protonic conductors as electrolytes in solid oxide fuel cells are the high temperature required to produce dense electrolytes, the high grain boundary electrical resistivity and the poor chemical stability under carbon dioxide, which may restrict the operation of fuel cells under carbon containing fuels (4), the same problem found when sintering using organic additives (8). The reported reasons for the high grain boundary resistivity are mainly the large density of interfaces resulting from the difficulty of increasing the average grain size at usually available ( $1400$ - $1600^\circ\text{C}$ ) sintering temperatures. Besides Y and Gd, there are many results on barium cerate proton conductors doped with other rare earth ions like Yb, Dy (9), Sm and Nd (10).  $\text{BaCeO}_3$  and  $\text{BaZrO}_3$  form solid solutions and a suitable fraction of Ce in  $\text{BaCeO}_3$  with Zr forms a solid solution that exhibits both adequate proton conductivity as well as sufficient chemical and thermal stability relevant to SOFC operation (11-14).  $\text{BaZr}_{0.1}\text{Ce}_{0.7}\text{Y}_{0.2}\text{O}_{3-\delta}$  (BZCY7) at temperatures below  $550^\circ\text{C}$  has one of the highest ionic conductivity of all known electrolyte materials for SOFC applications (14). Recently  $\text{BaZr}_{0.1}\text{Ce}_{0.7}\text{Y}_{0.2-x}\text{Yb}_x\text{O}_{3-\delta}$  compounds, a mixed proton and oxide ion conductor, was reported as exhibiting high ionic conductivity at relatively low temperatures ( $500^\circ$  to

700°C), and also an ability to resist deactivation by sulfur and coking, and enhanced water adsorption capability (15). We report here a series of experiments on barium cerate zirconate compounds doped with yttrium, ytterbium and dysprosium, looking for combining microstructural analysis and impedance spectroscopy

## Experimental

All specimens were prepared with BaCO<sub>3</sub> (Alfa Aesar), ZrO<sub>2</sub> (Alfa Aesar), CeO<sub>2</sub> (Aldrich), Y<sub>2</sub>O<sub>3</sub> (USA), Dy<sub>2</sub>O<sub>3</sub> (Aldrich) and Yb<sub>2</sub>O<sub>3</sub> (Aldrich). For the synthesis of each composition, 2 g of stoichiometric amounts of the starting materials were dried, mixed for 2 h (8 x 15 min attrition with 10 min intervals for avoiding excessive Joule heating and consequent particle sintering) in a homemade attritor operating at 220 rpm with 60 mL of 2 mm diameter Y-TZP milling media (Tosoh, Japan) and 15 mL of ethanol. The milling media were afterwards washed in ethanol and this solution was dried at 100°C/60 min plus 150°C/30 min and 100°C overnight for obtaining the comminuted powder mixture.

The thermogravimetric and the differential thermal analysis of all mixtures were carried out in a Netzsch Simultaneous Thermal Analyzer 409 C in air in the room temperature-1550°C range at 10°C/min heating/cooling rates.

The attrition milled powders of all compositions were heat treated at 1100°C / 10 h at a 10°C/min rate. X-ray diffraction experiments were carried out in a Bruker-AXS D8 Advance X-ray diffractometer with Ni-filtered  $\lambda_1$ - $\lambda_2$  Cu- $\kappa$  radiation in the 10-90° 2 $\theta$  range, 0.05° 2 $\theta$  step, 5 s per step.

Two samples of each composition were dried, attrition milled again in the same condition described above, dried, weighed (400 mg each), pressed (200 kgf/cm<sup>2</sup>) in 8 mm inner diameter cylindrical dies, plastic sealed under rough vacuum, isostatically pressed at 30 kpsi, and sintered at 1550°C/4 h with 5 deg/min heating and cooling rates. Pressures higher than 200 kgf/cm<sup>2</sup> caused lamination and cracking of the pellets during sintering. For sintering, a powder bed with a mixture of BaCO<sub>3</sub> and ZrO<sub>2</sub> was used. After sintering, the face of the pellet in contact with the powder bed turned light green and the opposite face dark green, probably due to the different partial pressures of oxygen.

The impedance spectroscopy measurements were carried out in a two-electrode cell configuration in the 200-700°C range with a Hewlett-Packard 4192A LF impedance analyzer connected to a HP 362 controller for collecting and analyzing the data. An Inconel 600 sample chamber with three spring-loaded platinum electrodes for holding three specimens was inserted in a programmable furnace. Platinum leads and a K-type thermocouple with its junction close to the specimens were used. The [- Z''( $\omega$ ) x Z'( $\omega$ )] impedance spectroscopy data were collected at constant temperatures in the 5 Hz to 13 MHz frequency range. Special software was used for collecting and analyzing these data (16). The deconvolution of the [- Z''( $\omega$ ) x Z'( $\omega$ )] diagrams was carried out to evaluate the intragranular (grain) resistance R<sub>g</sub> and the intergranular (grain boundary) resistance R<sub>gb</sub>.

The disk shaped specimens were cross-sectioned into 2 mm x 2 mm x 10 mm bar-shaped specimens. The face showing the bulk of the specimens was polished with silicon carbide powder and subsequently with diamond pastes down to 1  $\mu\text{m}$  average particle size. The polished specimens were thermally etched at 1450°C/20 min to observe the polished and etched surface in both a scanning probe microscope and a field-emission gun scanning electron microscope. The scanning probe microscope was a Jeol JSPM-5200 operating in contact mode for obtaining dynamic force topography images, 100  $\mu\text{m}$  x 100  $\mu\text{m}$  down to 100 nm x 100 nm scanning area. The FEG-SEM analyses were carried out in a Jeol JSM-6701F scanning electron microscope on a Pt-sputtered surface of the specimens. The observations with the two microscopes were done onto the same sample face. Platinum deposition by sputtering, required for FEG-SEM observation, was done on half surface by covering the other half with Teflon tape, removed for SPM observation.

## Results and Discussion

### Thermal Analysis

Figure 1 shows curves of the thermogravimetric analysis in air of the  $\text{BaCO}_3 + \text{ZrO}_2 + \text{CeO}_2 + \text{Y}(\text{Dy}, \text{Yb})_2\text{O}_3$  mixtures from room temperature to 1550°C for obtaining three specimens:  $\text{BaZr}_{0.1}\text{Ce}_{0.7}\text{Y}_{0.2}\text{O}_{3-\delta}$ ,  $\text{BaZr}_{0.1}\text{Ce}_{0.7}\text{Dy}_{0.2}\text{O}_{3-\delta}$ , and  $\text{BaZr}_{0.1}\text{Ce}_{0.7}\text{Yb}_{0.2}\text{O}_{3-\delta}$ . The behavior is similar: a decrease in the mass in the 800-1100°C temperature range due to the expected 12% mass reduction in the decomposition of barium carbonate to barium oxide. The endothermic peak at 803°C is due to the  $\alpha$  orthorhombic, *Pm $\bar{c}n$* , to the  $\beta$  trigonal, *R $\bar{3}m$* , phase transition of the barium carbonate (17). The mixture containing Dy presents a somewhat different behavior in the 200-400°C during heating. A noticeable step down in the DTA signal is found during cooling the Y-doped (at 439°C), the Yb-doped (404°C) and the Dy-doped (390°C) specimens, probably due to structural phase transition. In situ X-ray diffraction experiments will be performed to verify this hypothesis.

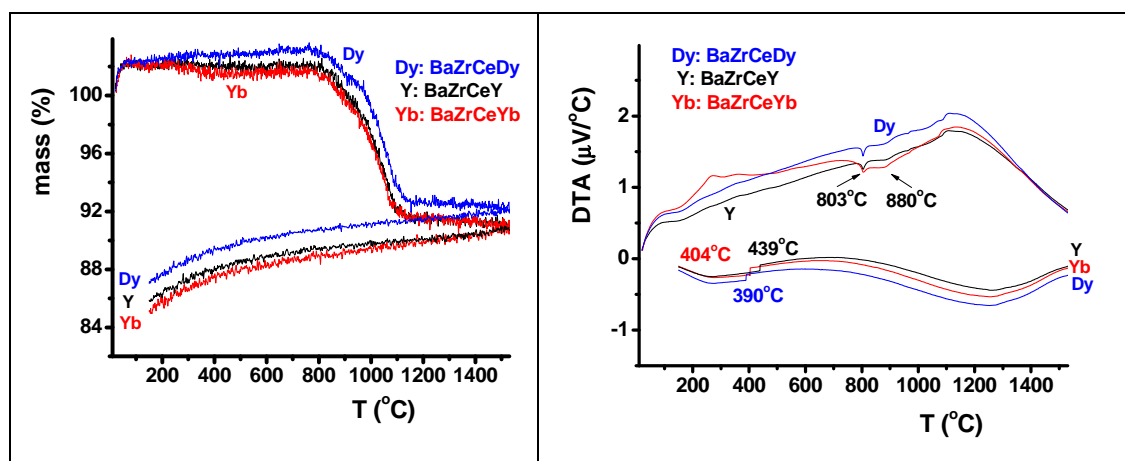


Figure 1. Mass variation (left) and differential thermal analysis (right) curves of the reaction of  $\text{BaCO}_3$ ,  $\text{ZrO}_2$ ,  $\text{CeO}_2$  and  $\text{Y}_2\text{O}_3$  or  $\text{Dy}_2\text{O}_3$  or  $\text{Yb}_2\text{O}_3$  during heating up to 1550°C and down to 100°C for preparing  $\text{BaZr}_{0.1}\text{Ce}_{0.7}\text{Y}_{0.2}\text{O}_{3-\delta}$ ,  $\text{BaZr}_{0.1}\text{Ce}_{0.7}\text{Dy}_{0.2}\text{O}_{3-\delta}$ , and  $\text{BaZr}_{0.1}\text{Ce}_{0.7}\text{Yb}_{0.2}\text{O}_{3-\delta}$  compounds. Heating and cooling rates: 10 deg/min.

Instead of the single substitution of Dy or Yb for Y, double doping was done by partial substitution of Dy (0.1 mol) and Yb (0.1 mol) for Y, keeping 0.1 mol Y. Figure 2 shows curves of the thermogravimetric and differential thermal analyses of  $\text{BaCO}_3 + (0.1) \text{ZrO}_2 + (0.7) \text{CeO}_2 + (0.1) \text{Y}_2\text{O}_3$ ,  $\text{BaCO}_3 + (0.1) \text{ZrO}_2 + (0.7) \text{CeO}_2 + (0.1) \text{Dy}_2\text{O}_3$  and  $\text{BaCO}_3 + (0.1) \text{ZrO}_2 + (0.7) \text{CeO}_2 + (0.05) \text{Y}_2\text{O}_3 + (0.05) \text{Dy}_2\text{O}_3$ .

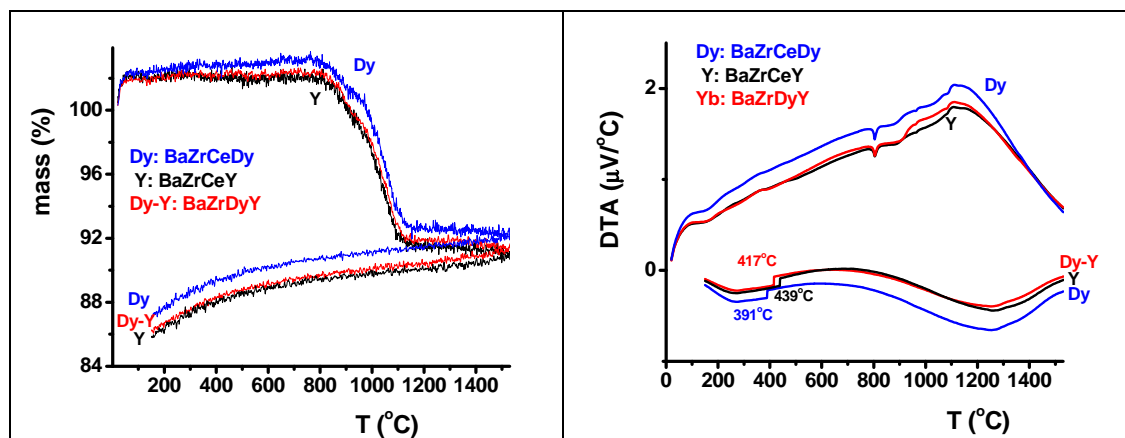


Figure 2. Mass variation (left) and differential thermal analysis (right) curves of the reaction of  $\text{BaCO}_3$ ,  $\text{ZrO}_2$ ,  $\text{CeO}_2$  and  $\text{Y}_2\text{O}_3$  or  $\text{Dy}_2\text{O}_3$  or  $\text{Y}_2\text{O}_3$ - $\text{Dy}_2\text{O}_3$  during heating up to  $1550^\circ\text{C}$  and down to  $100^\circ\text{C}$  for preparing  $\text{BaZr}_{0.1}\text{Ce}_{0.7}\text{Y}_{0.2}\text{O}_{3-\delta}$ ,  $\text{BaZr}_{0.1}\text{Ce}_{0.7}\text{Dy}_{0.2}\text{O}_{3-\delta}$ , and  $\text{BaZr}_{0.1}\text{Ce}_{0.7}\text{Y}_{0.1}\text{Dy}_{0.1}\text{O}_{3-\delta}$  compounds. Heating and cooling rates: 10 deg/min.

Figure 3 shows curves of the thermogravimetric and differential thermal analyses of  $\text{BaCO}_3 + (0.1) \text{ZrO}_2 + (0.7) \text{CeO}_2 + (0.1) \text{Y}_2\text{O}_3$ ,  $\text{BaCO}_3 + (0.1) \text{ZrO}_2 + (0.7) \text{CeO}_2 + (0.1) \text{Dy}_2\text{O}_3$  and  $\text{BaCO}_3 + (0.1) \text{ZrO}_2 + (0.7) \text{CeO}_2 + (0.05) \text{Y}_2\text{O}_3 + (0.05) \text{Dy}_2\text{O}_3$ .

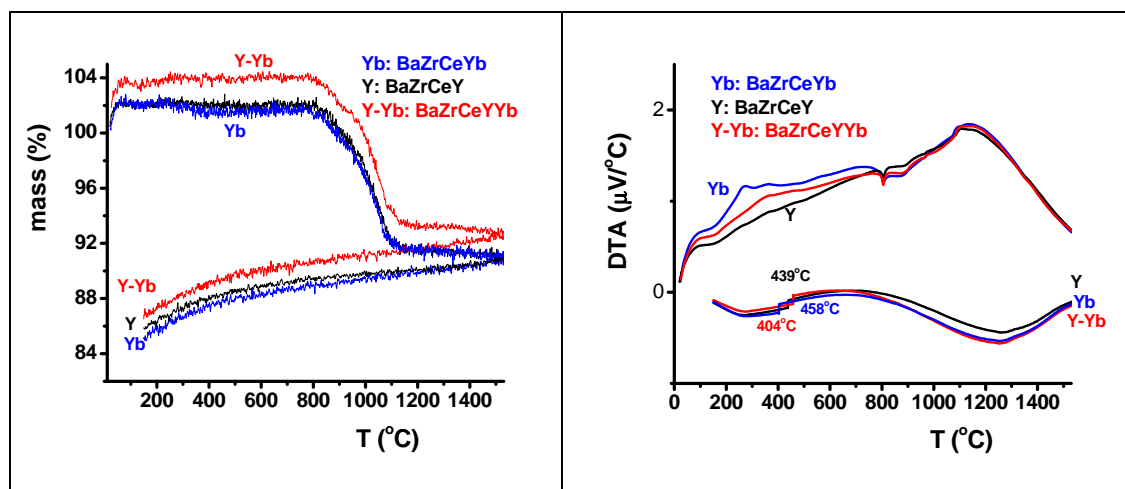


Figure 3. Mass variation (left) and differential thermal analysis (right) curves of the reaction of  $\text{BaCO}_3$ ,  $\text{ZrO}_2$ ,  $\text{CeO}_2$  and  $\text{Y}_2\text{O}_3$  or  $\text{Yb}_2\text{O}_3$  or  $\text{Y}_2\text{O}_3$ - $\text{Yb}_2\text{O}_3$  during heating up to  $1550^\circ\text{C}$  and down to  $100^\circ\text{C}$  for preparing  $\text{BaZr}_{0.1}\text{Ce}_{0.7}\text{Y}_{0.2}\text{O}_{3-\delta}$ ,  $\text{BaZr}_{0.1}\text{Ce}_{0.7}\text{Yb}_{0.2}\text{O}_{3-\delta}$ , and  $\text{BaZr}_{0.1}\text{Ce}_{0.7}\text{Y}_{0.1}\text{Yb}_{0.1}\text{O}_{3-\delta}$  compounds. Heating and cooling rates: 10 deg/min.

### X-ray Diffraction Analyses

The samples remaining in the alumina crucible after the TG/DTA measurements described above were analyzed by X-ray diffraction. The results are shown in Figure 4.

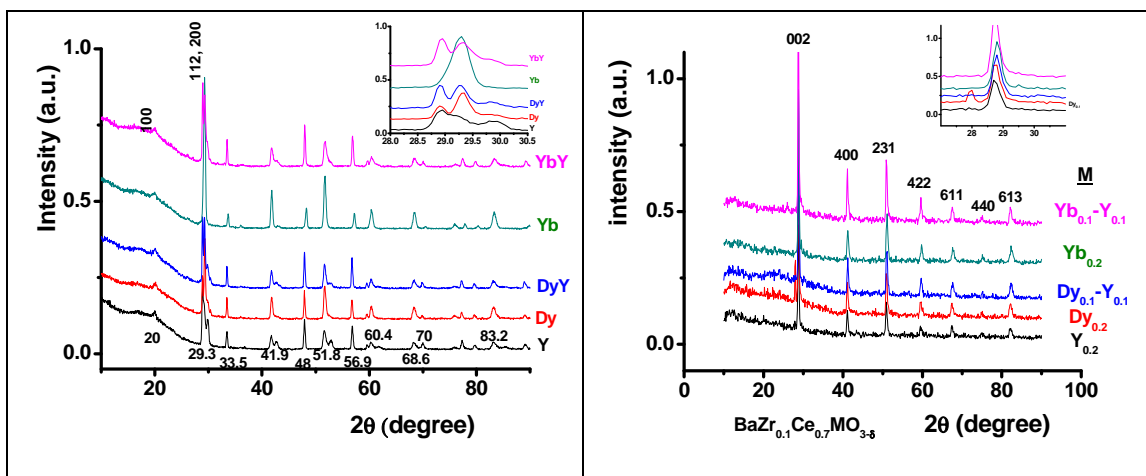


Figure 4. X-ray diffraction patterns of  $\text{BaZr}_{0.1}\text{Ce}_{0.7}\text{Y}_{0.2}\text{O}_{3-\delta}$ ,  $\text{BaZr}_{0.1}\text{Ce}_{0.7}\text{Dy}_{0.2}\text{O}_{3-\delta}$ ,  $\text{BaZr}_{0.1}\text{Ce}_{0.7}\text{Y}_{0.1}\text{Dy}_{0.1}\text{O}_{3-\delta}$ ,  $\text{BaZr}_{0.1}\text{Ce}_{0.7}\text{Yb}_{0.2}\text{O}_{3-\delta}$ , and  $\text{BaZr}_{0.1}\text{Ce}_{0.7}\text{Y}_{0.1}\text{Yb}_{0.1}\text{O}_{3-\delta}$  compounds. Left: powders; Right: sintered pellets. Inset: zoom of the 28.0-30.5  $2\theta$  range.

The diffraction patterns of the powders are typical of the orthorhombic perovskite phase of the  $\text{BaCeO}_3$  compound (JCPDS 22-0074 and ICSD 043135) while the ones of the pellets are typical of the cubic perovskite phase of the  $\text{BaCeO}_3$  compound (18). Symmetry of the  $\text{BaCe}_{0.9-x}\text{Zr}_x\text{Y}_{0.1}\text{O}_{3-\delta}$  lattice was reported to be orthorhombic at  $0 \leq x \leq 0.2$  and cubic at  $0.3 \leq x \leq 0.9$  (11), meaning that varying Zr and Y content may lead to both orthorhombic and cubic structures.

### Impedance Spectroscopy Analyses

Figure 5 shows impedance diagrams of (a)  $\text{BaZr}_{0.1}\text{Ce}_{0.7}\text{Y}_{0.2}\text{O}_{3-\delta}$ , (b)  $\text{BaZr}_{0.1}\text{Ce}_{0.7}\text{Dy}_{0.2}\text{O}_{3-\delta}$  and (c)  $\text{BaZr}_{0.1}\text{Ce}_{0.7}\text{Yb}_{0.2}\text{O}_{3-\delta}$  pellets at  $260^\circ\text{C}$ . It is apparent the huge semicircles arc due to blocking of charge carriers at interfaces.

Figure 6 shows impedance diagrams of the  $\text{BaZr}_{0.1}\text{Ce}_{0.7}\text{Y}_{0.2}\text{O}_{3-\delta}$ ,  $\text{BaZr}_{0.1}\text{Ce}_{0.7}\text{Dy}_{0.2}\text{O}_{3-\delta}$  and  $\text{BaZr}_{0.1}\text{Ce}_{0.7}\text{Yb}_{0.2}\text{O}_{3-\delta}$  sintered pellets measured at two different temperatures,  $160^\circ\text{C}$  and  $260^\circ\text{C}$ . The diagrams have in common the relatively very large intergranular (grain boundary) resistivity when comparing to the intragranular (bulk) resistivity (cf. Figure 5). This is a common feature to barium cerate, barium zirconate and barium cerate zirconate compounds, when sintered at temperatures not high enough to eliminate part of the interfaces, mainly grain boundaries, through grain growth. In the  $[-Z''(\omega) \times Z'(\omega)]$  impedance diagram of  $\text{BaZr}_{0.1}\text{Ce}_{0.7}\text{Y}_{0.2}\text{O}_{3-\delta}$  measured at  $260^\circ\text{C}$ , a calculation yielded  $6.5 \times 10^{-12} \text{ F/cm}$  and  $4 \times 10^{-9} \text{ F/cm}$  for the high frequency and the low frequency semicircles, respectively. These values are typical of specific intragranular (bulk) and intergranular (grain boundary) capacitances (19).

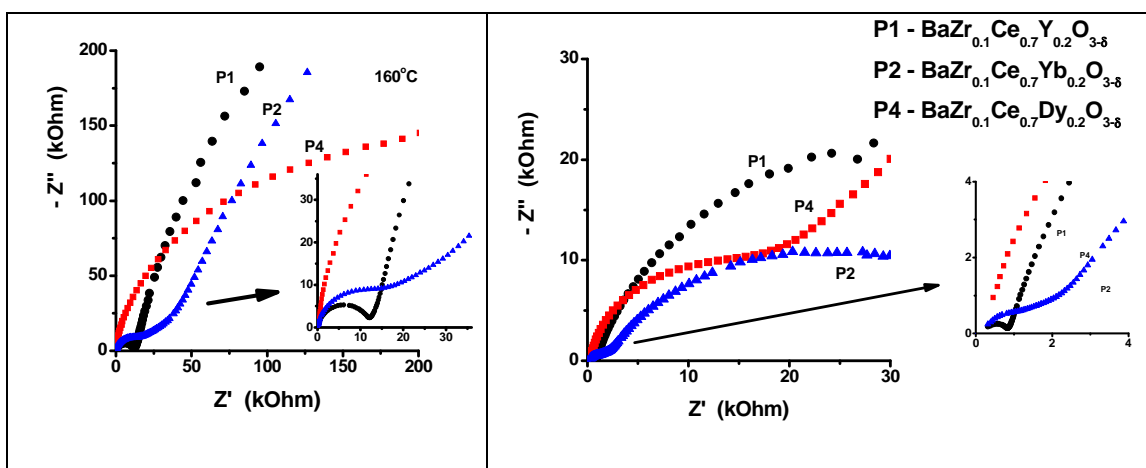
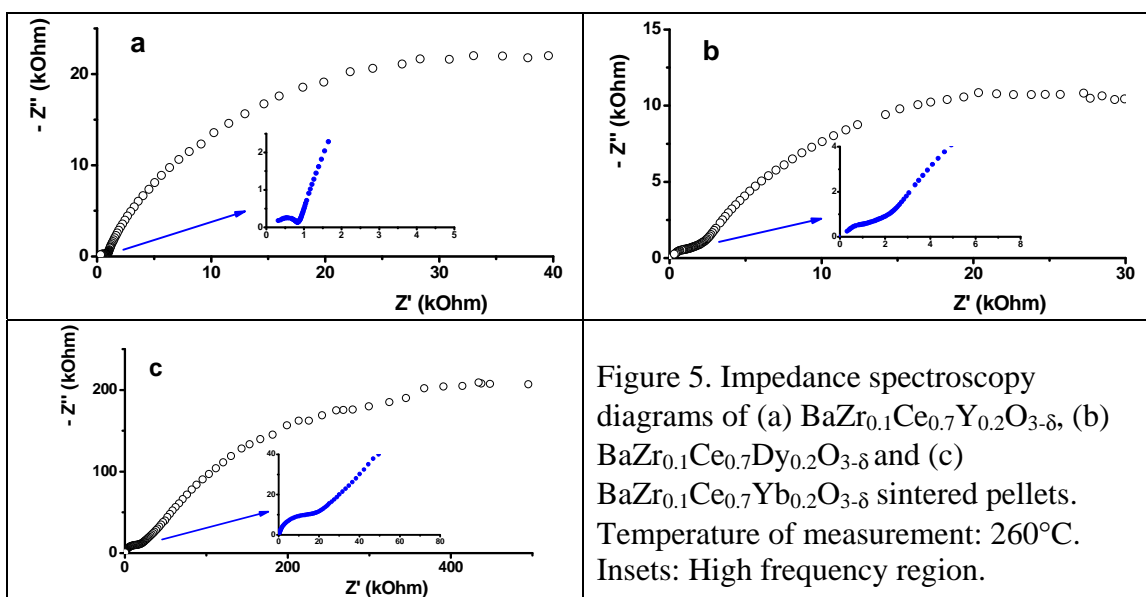


Figure 6. Impedance spectroscopy diagrams of  $\text{BaZr}_{0.1}\text{Ce}_{0.7}\text{Y}_{0.2}\text{O}_{3-\delta}$ ,  $\text{BaZr}_{0.1}\text{Ce}_{0.7}\text{Dy}_{0.2}\text{O}_{3-\delta}$  and  $\text{BaZr}_{0.1}\text{Ce}_{0.7}\text{Yb}_{0.2}\text{O}_{3-\delta}$  sintered pellets. Temperature of measurement: left: 160°C; right: 260°C. Insets: High frequency region.

### Surface Analysis by SEM and SPM

Scanning electron microscopy and scanning probe microscopy analyses of polished and thermally etched surfaces of the single-doped (Y, Dy, or Yb) sintered pellets were obtained. Figure 7 shows the typical images. The Field Emission Gun SEM micrographs show interesting features: the  $\text{BaZrCeY}$  compound has grains in the micron region, but many sub-grain like structures inside them (Fig. 7a). The corresponding topographic image obtained by SPM (Fig. 7b) shows details of the interfaces inside the grains. The results for  $\text{BaZrCeDy}$  are similar, but present an additional feature: the intergranular region is filled up with small spherical grains. A chemical analysis of this intergranular region shows that dysprosium is the main component. This means that 2 mol% of dysprosium is larger than its solubility limit in the barium cerate zirconate matrix, motivating its segregation at the grain boundaries, inhibiting grain growth and hence

helping to explain the large intergranular component of the electrical resistivity measured by impedance spectroscopy. Ytterbium doping (Figs. 7e and 7f) shows images similar to the ones with yttrium doping.

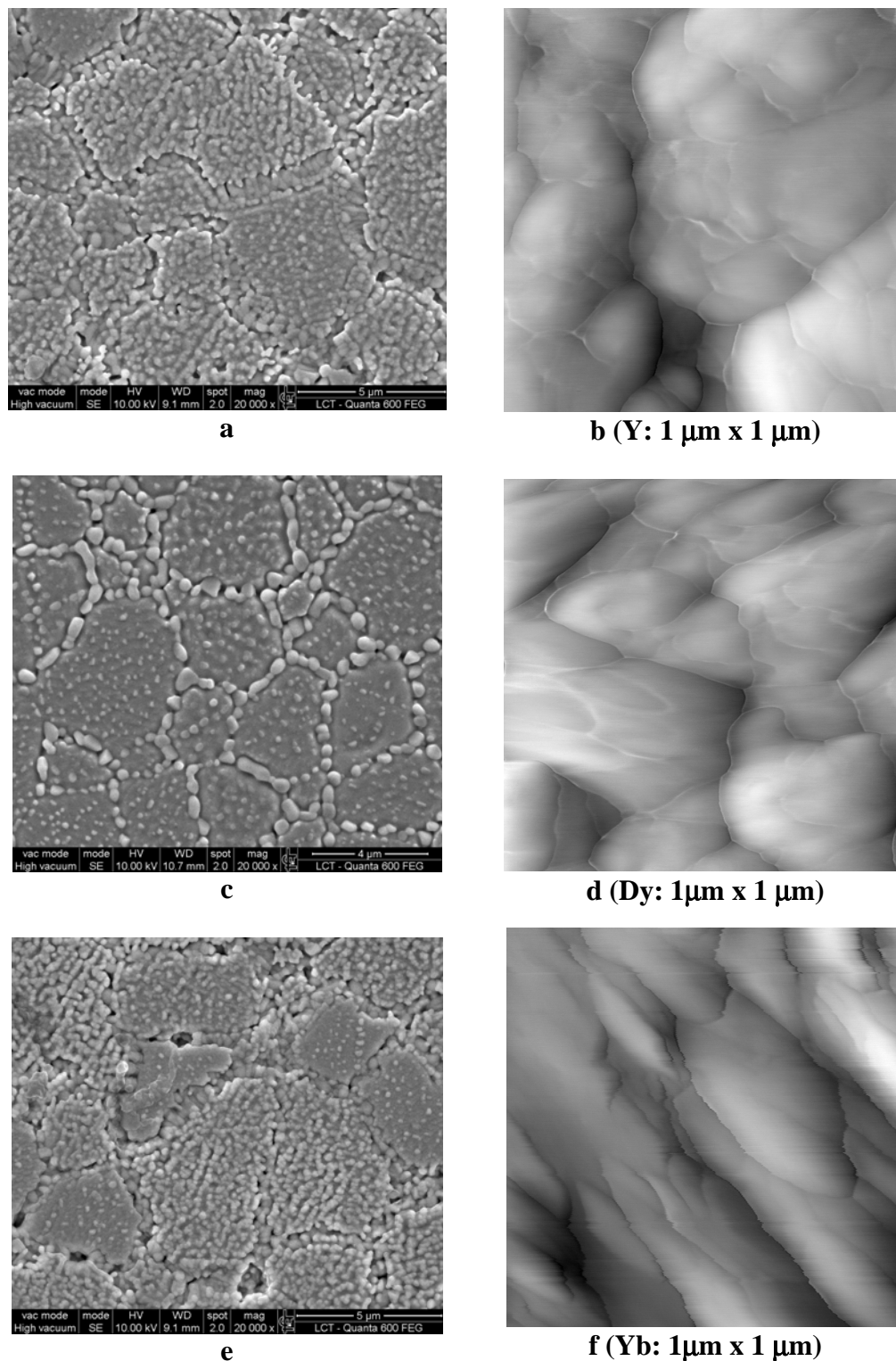


Figure 7. SEM (a, c, e, left) and SPM (b, d, f, right) images of BaZr<sub>0.1</sub>Ce<sub>0.7</sub>Y<sub>0.2</sub>O<sub>3-δ</sub> (top), BaZr<sub>0.1</sub>Ce<sub>0.7</sub>Dy<sub>0.2</sub>O<sub>3-δ</sub> (middle) and BaZr<sub>0.1</sub>Ce<sub>0.7</sub>Yb<sub>0.2</sub>O<sub>3-δ</sub> (bottom) surfaces of sintered pellets.

## Conclusions

Barium cerate zirconate protonic conductors, synthesized by single doping with yttrium, dysprosium, ytterbium and double doping with yttrium-dysprosium and yttrium-ytterbium, show high intergranular electrical resistivity in the RT-500°C temperature range due mainly to interfaces inside the grains. These interfaces were observed in high resolution scanning probe microscopy images.

## Acknowledgments

To FAPESP (Proc. 05/53241-9) for financial support. To Yone V. França for the preparation of the specimens.

## References

1. T. Takahashi and H. Iwahara, *Rev. Chim. Miner.*, **17**, 243 (1980).
2. H. Iwahara, T. Esaka, H. Uchida and N. Maeda, *Solid State Ionics*, **3-4**, 359 (1981).
3. H. Iwahara, H. Uchida, K. Ono and J. Ogaki, *J. Electrochem. Soc.*, **135**, 529 (1988).
4. N. Bonanos, K. S. Knight and B. Ellis, *Solid State Ionics*, **79**, 161 (1995).
5. T. Norby, *Solid State Ionics*, **125**, 1 (1999).
6. K. D. Kreuer, *An. Rev. Mater. Res.*, **33**, 333 (2003).
7. T. Norby, M. Widerøe, R. Glöckner and Y. Larring, *Dalton Trans.*, **19**, 3012 (2004).
8. M. J. Scholten, J. Schoonman, J. C. van Miltenburg and H. A. J. Oonk, *Solid State Ionics*, **61**, 83 (1993).
9. W. B. Wang, J. W. Liu, Y. D. Li, H. T. Wang, F. Zhang and G. L. Ma, *Solid State Ionics*, **181**, 667 (2010).
10. H. Iwahara, T. Hibino and M. Yamada, in *Proc. of the 3<sup>rd</sup> International Symposium on Solid Oxide Fuel Cell*, Honolulu, **93-94**, p. 137 (1993).
11. K. Katahira, Y. Kohchi, T. Shimura and H. Iwahara, *Solid State Ionics*, **138**, 91 (2000).
12. K. H. Ryu and S. M. Haile, *Solid State Ionics*, **125**, 355 (1999).
13. C. Zuo, T. H. Lee, S.-J. Song, L. Chen, S. E. Dorris, U. Balachandran and M. Liu, *Electrochem. Solid State Lett.*, **8**, J35 (2005).
14. C. Zuo, S. Zha, M. Liu, M. Hatano and M. Uchiyama, *Adv. Mater.* **18** (24), 3318 (2006).
15. L. Yang, S. Wang, K. Blinn, M. Liu, Z. Liu, Z. Cheng and M. Liu, *Science*, **326**, 126 (2009).
16. M. Kleitz and J. H. Kennedy, in *Fast Ion Transport in Solids*, P. Vashishta, J. N. Mundy and G. K. Shenoy, Editors, p. 185, Elsevier North Holland, The Netherlands (1979).
17. S. M. Antao and I. Hassan, *Phys. Chem. Minerals*, **34**, 573 (2007).
18. H. Ding and X. Xue, *J. Power Sources*, **195**, 7038 (2010).
19. J. G. Fletcher, A. R. West and J. T. S. Irvine, *J. Electrochem. Soc.* **142**, 2650 (1995).